Relationship between Proton Transport and Morphology of Perfluorosulfonic Acid Membranes: A Reactive Molecular Dynamics Approach

doi: 10.1021/acs.jpcb.8b02318

Relationship between Proton Transport and Morphology of Perfluorosulfonic Acid Membranes: A Reactive Molecular Dynamics Approach

Takuya MABUCHI[1, *] *and Takashi TOKUMASU*[2]

[1]Frontier Research Institute for Interdisciplinary Sciences, Tohoku University, 2-1-1 Katahira Aoba-ku, Sendai, Miyagi 980-8577, Japan

[2]Institute of Fluid Science, Tohoku University, 2-1-1 Katahira Aoba-ku, Sendai, Miyagi 980-8577, Japan

Corresponding author

*E-mail: mabuchi@tohoku.ac.jp

ABSTRACT

A reactive molecular dynamics simulation has been performed for the characterization of the relationship between proton transport and water clustering in polymer electrolyte membranes. We have demonstrated that the anharmonic two-state empirical valence bond (*a*TS–EVB) model is capable of describing efficiently excess proton transport through the Grotthuss hopping mechanism within the simplicity of the theoretical framework. In order to explore the long-time diffusion behavior in PFSA membranes with statistical certainty, simulations that are longer than 10 ns are needed. The contribution of the Grotthuss mechanism to the proton transport yields a larger fraction compared to the vehicular mechanism when the estimated percolation threshold of $\lambda = 5.6$ is surpassed. The cluster analyses elicit a consistent outlook in regard to the relationship between the connectivity and confinement of water clusters and proton transport. The cluster growth behavior findings reveal that below the percolation threshold, the water domains grow along the channel length to form the connected elongated clusters, thus contributing to an increase in connectivity and a decrease in confinement, whereas above the percolation threshold the channel widths of water domains increase, while the elongated structure of clusters is retained, thereby contributing to further confinement decreases.

1. INTRODUCTION

Polymer electrolyte fuel cells (PEFCs) have been developed as highly efficient and clean energy sources for use in transportation. Perfluorosulfonic acid (PFSA) membranes, such as Nafion developed by DuPont, are currently the principal electrolyte and separator materials adopted for use as polymer electrolyte membranes (PEMs). The efficiency of proton transport in PEMs is one of the key factors that dominate power generation efficiency. Previous research studies have revealed the difficulties associated with the structural and dynamical properties of protons based on macroscopic simulations in accordance to continuum theory because proton transport is largely influenced by the morphology of the membrane, as well as by the surrounding environment of water molecules at the nanoscale.[1, 2] Thus, attention has focused on the understanding of the fundamental processes involved in proton transport within the nanoscopic confined water environment of hydrated PFSA membranes.

PFSA membranes consist of a hydrophobic polytetrafluoroethylene backbone and hydrophilic sulfonate group side chains, which form microphase-separated higher-order structures. Proton conductivity and the transport mechanism in PFSA membranes largely depends on the hydration level of the membrane.[3-6] As the hydration level increases, the hydrophilic domains swell significantly and create continuous paths for proton conduction. The proton hopping mechanism, known as the Grotthuss mechanism,[7] has been considered as a key process that can be used to explain some experimental results regarding proton transport in PFSA membranes,[5] although the complexity of the process means that the details of the Grotthuss mechanism remain unclear.

Theoretical approaches, including molecular dynamics (MD) simulations and ab initio calculations, have been extensively used to study proton transport and morphology of PFSA

membranes.[8-27] Most of these studies,[8-19] however, employ classical hydronium cation models that do not incorporate the Grotthuss mechanism and thus lack the essential physics fundamentals of proton transport. For this reason, proton transport properties including the Grotthuss mechanism have been studied using reactive molecular dynamics (RMD) approaches such as empirical valence bond (EVB) methods,[20-27] which allow dynamic breaking and formation of O–H chemical bonds. Feng and Voth[20] used the self-consistent multistate EVB (SCI–MS–EVB) method to study the mechanism of proton transport in hydrated Nafion. The authors found that a proton hopping mechanism becomes more significant for proton transport as the water content λ (the number of hydronium ions and water molecules per sulfonate group of the PFSA side chain) increases from 6 to 15, and indicated there is a certain degree of anticorrelation with the vehicular transport. Savage and Voth[24] showed that the caging effects of protons last at least ~1 ns in PFSA systems, which reveals the presence of substantial subdiffusive behavior of proton transport in the typical simulation time of 1–2 ns used in previous studies of PFSA membrane systems.[20-23] Selvan et al.[28] have developed an analytical model, which is based on the confined random walk (CRW) simulation approach,[29] and allowed one to generate mean square displacements (MSDs) out up to 100 ns from the short-time MD results for the prediction of proton diffusions in PEMs. However, the model does not fully describe the accurate proton transport mechanism, such as the intrinsic nature of negative correlation between vehicular and structural components. Therefore, to fully explore the long-time diffusive behavior directly with statistical certainty, it is suggested that multiple nanosecond trajectories are needed, which have been limited to a certain degree by the MS–EVB approaches since a large number of EVB states are required. Alternatively, the two-state EVB (TS–EVB) approaches[30, 31] provide an efficient and reasonable description of proton transport properties within the simplified theoretical framework in comparison to the multistate EVB algorithm, even though the MS–EVB approaches are more elaborate and physically accurate,

particularly in terms of polarizability. Since only one water molecule—the closest to the hydronium ion—is assigned as the partner for proton transfer during the transfer process in TS-EVB approaches, there is a restriction in terms of the charge delocalization effect beyond the partner cluster of the Zundel cation, which may be particularly important for vibrational spectra.[32] The anharmonic TS–EVB (*a*TS–EVB) model[31] is a modified version of the TS–EVB model developed by Walbran and Kornyshev[30] (WK model). In this model, the local nature of the charge switching function algorithm allows the EVB complexes for each proton to be handled independently. Thus, the computational cost can scale linearly with respect to the number of protons within the two-state EVB approaches. These features clearly satisfy the requirement of longer simulations to understand the long-time diffusive behavior of protons in PFSA systems within the limits of available computational capabilities.

Since the nanophase-segregated structures in PFSA membranes affect proton diffusivity through a PEM, it is reasonable to believe that the intrinsic nature and mechanism of proton transport are strongly affected by the PFSA membrane morphology. Kuo et al. have investigated the effect of water content on the morphology of the PFSA membrane using classical MD simulations, and found that the morphology of the water domains changes with increasing water content from a channel network structure to a tortuous layered structure.[18] Liu et al.[19] have performed classical MD simulations to investigate the hydrated morphology of PFSA membranes in terms of connectivity and confinement of hydrophilic water domains. They have suggested that the diffusivity is controlled by the balance between the connectivity and confinement of the water domains. Based on intuitive expectations, better connectivity of water clusters should result in a higher diffusivity of protons because an efficient aggregation of clusters gives rise to additional continuous paths. Conversely, more confinement (i.e., smaller channels) should result in a lower diffusivity because the smaller channel size (such as the width and length) limits the proton

transport pathway. Understanding the impacts of these effects is critical to clarify the relationship between proton transport and the morphology of PFSA membranes. Selvan et al.[28] have predicted the water diffusivity in PEMs well compared to experimental data using an analytical model based on MD and CRW simulations. The authors have demonstrated that accounting for three factors, including acidity (i.e., water content), confinement, and connectivity, is important and sufficient to understand the water diffusive behavior in PEMs. In the model, the three factors of acidity, confinement, and connectivity, are characterized by the volume of the water domain, surface area, and cluster connectivity, respectively.

In the present work, an RMD simulation has been performed to investigate further the relationship between proton transport and water clustering. The aims of this study are to: (i) provide a more in-depth picture of the distinct cluster growth behaviors below and above the percolation threshold that influence the contributions of connectivity and confinement to proton transport, and (ii) demonstrate applicability of the *a*TS–EVB model to fully explore the long-time diffusive behavior and reproduce quantitatively the experimental values of proton/water self-diffusivity, as well as the intrinsic nature of proton solvation and transport mechanism observed in previous RMD simulations.[20, 21] Our simulations provide direct, detailed quantitative information on the correlation between the proton transport properties and the water cluster structures, which to our knowledge has not been fully defined previously.

2. SIMULATION DETAILS

The present simulation systems were composed of eight PFSA chains, representative of Nafion with equivalent weights of approximately 1150. Each chain consisted of 10 hydrophilic side chains terminated with SO_3^- moieties and spaced evenly by seven nonpolar $–CF_2CF_2–$

monomers that formed a hydrophobic backbone. It was assumed that all the protons are fully dissociated from the sulfonate groups and form hydronium ions at $\lambda \geq 3$ based on the report of Wang et al.[33] The Nafion potential from our previous study,[15] which was based on the DREIDING force field,[10, 34, 35] was used in the present work. The *a*TS–EVB model[31] was employed given the potential of water molecules and excess protons to incorporate the Grotthuss mechanism in multiproton environments. Although the damped charges for the hydronium ion (total charges of +0.7*e*) are used in the *a*TS–EVB model, this can be rationalized by the strong delocalization of charges and by the possibility of charge transfer from the hydronium ion to its surroundings in hydrated Nafion membranes.[36, 37] A significant charge transfer was observed in the quantum mechanical calculation of PFSA membranes, wherein charges of +0.68*e* in the cluster and +0.72*e* in the crystal were reported for the hydronium ion according to Mulliken population analyses.[36] However, as the current model limits the full ionic charge transfer, incorporation of electronic polarization effects into the present model is desirable to reproduce the full-charge transition process in the EVB complex, which will be a focus for future *a*TS–EVB model developments. The Lorentz–Berthelot mixing rules were used for the interactions between different types of atoms, while the smooth particle mesh Ewald method[38] with a precision of 10^{-6} was used to calculate electrostatic interactions. The r–RESPA algorithm[39] was used to integrate the equations of motion with a large timestep of 2.0 fs, while the small timestep of 0.5 fs was used for the intramolecular interactions. The temperature was kept constant using the Nosé–Hoover thermostat[40, 41] and the pressure was controlled using the Andersen method.[42]

The initial configurations were generated by placing eight Nafion chains randomly in a simulation box. A periodic boundary condition was applied in all directions. A total of 80 (8 chains × 10 sulfonate groups per chain) hydronium ions were then added to maintain charge

neutrality and the membrane was hydrated by adding water molecules corresponding to a given λ. In this study, we considered water contents of λ = 3, 5, 7, 12, and 20. All of the systems were first equilibrated with the annealing procedure developed in the previous study[15] by using the classical hydronium ion model to obtain the equilibrated structures at the desired pressure of 1 Atm and at a temperature of 300 K. Subsequently, canonical (*NVT*) simulations were carried out for 500 ps at 300 K to relax the system further under the *a*TS–EVB potential. The final structures for each system were then used for production runs of 20 ns in the constant *NVE* ensemble, and the trajectory of molecules was acquired every 0.1 ps.

3. RESULTS AND DISCUSSION

3.1. Proton solvation structures

The proton solvation structure is largely influenced by the nearby sulfonate groups in PFSA membranes, thus resulting in a different proton diffusion mechanism from that in bulk water systems because of the negatively charged sulfonate groups.[20] Therefore, the proton and water distributions in the vicinity of the sulfonate group constitute important information. Figure 1 (a) shows the radial distribution functions (RDFs) between the sulfur atoms and the most hydronium-like oxygen O_h ($g_{S–Oh}$) at various water contents. As the first peak and first minimum are found to be at ~4.0 Å and ~4.4 Å, respectively, the distance of 4.4 Å is used to define the first solvation shell of the sulfonate groups. This result is very similar to the first minimum of ~4.3 Å obtained by the SCI–MS–EVB model, while the classical hydronium ion model indicates the first minimum at ~4.7 Å.[9, 15] The agreement between the *a*TS–EVB model and the SCI–MS–EVB model suggests that a weaker electronic interaction due to the damped charge in the *a*TS-EVB model is a good approximation for the charge delocalization effects in the SCI–MS–EVB model

on the electronic interaction between the sulfonate groups and the hydronium ions, as well as between the hydronium ions and water molecules in bulk water, as shown in our previous study.[31]

Figure 1 (b) shows the RDFs between O_h and the water oxygen atoms ($g_{Oh–Ow}$) at λ = 7. The hydronium ions are divided into two groups: the first group contains the hydronium ions in the first solvation shell, whereas the other contains the rest. The results show strong narrow peaks at 2.5 Å with the first minimum at ~2.9 Å for both groups. The coordination numbers within the first minimum (i.e., the number of first-shell water molecules around the hydronium ion) are calculated to be 1.9 and 3.0 in the first solvation shell and outside of the shell, respectively. The results indicate that protons are stabilized in the Eigen-like solvation structure beyond the first solvation shell, as observed in bulk water, whereas those present in the first solvation shell are strongly influenced by the sulfonate groups. When the proton is strongly bounded to the sulfonate group, the interaction between the proton and its surrounding water is weakened, thus resulting in the formation of proton solvation structure with less than three water molecules. Similar results were found for all λ values in the studied water content range.

3.2. Water cluster distributions and percolation

To obtain quantitative information about the characteristics of water clusters, the water cluster distributions were examined at different water contents. At increasing hydration levels, the morphology of the membrane is believed to exhibit a percolation transition from isolated hydrophilic water clusters to the three-dimensional network of water channels. The minimum water content, where the existence of spanning water clusters may be expected, can be described as the percolation threshold within the framework of percolation theory. The percolation threshold can be used as an important indicator of connectivity that ensures the presence of continuous proton pathways. The percolation behavior of water clusters was thus also investigated. In this

study, we considered hydronium ions and water molecules as part of the same cluster if their interoxygen distance was less than 3.5 Å, which is essentially the position of the first minimum in the oxygen–oxygen radial distribution functions for water molecules in bulk water.[31]

The cluster size distribution, n_s, defined as the probability of finding a cluster with size S (the number of hydronium ions and water molecules in a cluster), is shown in Figure 2. At the percolation threshold, n_s adheres to a power law dependence, whereby $n_s \sim S^{-\tau}$, with the three-dimensional universal exponent $\tau = 2.19$ for a wide range of S.[43] At $\lambda = 3$, n_s decreases rapidly with increases in S, and a large negative deviation from the power law is observed, which indicates that this water content is well below the percolation threshold. At $\lambda = 5$ and $\lambda = 7$, n_s can be fitted to the widest range of S with $\tau = 1.6$ and $\tau = 2.19$, respectively. Moreover, for $\lambda = 7$, n_s shows a sharp increase near the highest possible S, which is a feature that is usually related to conditions in which the water content exceeds the threshold value.[44] Therefore, the percolation threshold should lie within the water content range characterized by $\lambda = 5$ and $\lambda = 7$. For $\lambda = 12$ and $\lambda = 20$, that is, for values that are clearly above the percolation threshold, n_s elicits a spike near the highest possible S of ~950 and ~1590, respectively, which indicates the formation of a spanning cluster with a high connectivity of water molecules.

The percolation threshold can also be studied by calculating the mean cluster size, which is defined to be $S_{\text{mean}} = \sum n_s S^2 / \sum n_s S$ (the largest cluster is excluded from the sum). In finite systems, S_{mean} passes through a maximum just below the percolation threshold.[45-47] A plot of S_{mean} as a function of λ is shown in Figure 3. While S_{mean} shows a sharp increase from $\lambda = 3$ to $\lambda = 5$ because the clusters start to become larger, S_{mean} decreases at increasing water content from $\lambda = 7$ to $\lambda = 20$. Based on the percolation theory, these results thus show that the percolation threshold lies between $\lambda = 5$ and $\lambda = 7$. This indicates that larger intermediate-sized clusters are more likely to

be unstable and are absorbed into the largest cluster at λ values above the percolation threshold. Consequently, at high water contests of λ = 12 and λ = 20, S_{mean} shows the values of 2.7 and 2.0, respectively, which are relatively small compared to the largest possible cluster size (i.e., ~950 and ~1590 at λ = 12 and λ = 20, respectively), as observed in Figure 2.

To locate the percolation threshold, the probability, *R*, of finding an infinite cluster was examined, i.e., a cluster that spans the periodic simulation box in at least one dimension. The criterion that the probability of finding an infinite cluster was 50% was used to identify the percolation threshold.[46] The change of *R* with water content λ is shown in Figure 4. The fit of the simulation data to the Boltzmann sigmoidal function (solid red line) identifies a percolation threshold at λ = 5.6, which is consistent with an abrupt change in the dielectric constant of Nafion at approximately λ = 6, as documented in the experimental work of Lu et al.[48] and in our estimations described earlier. Therefore, these results provide consistent evidence of water percolation at λ = 5.6 in the studied PFSA membrane. Snapshots of the water cluster network in the membrane at λ = 5, 7, and 12 are shown in Figure 5. For clarity, each cluster is shown with a different color (the largest cluster is shown in white) and the Nafion chains are not shown. At λ = 5, small isolated clusters can be observed, whereas at λ = 7, clusters grow to intermediate sizes, including spanning clusters, which are frequently connected and disconnected by transient water bridges. At λ = 12, a large spanning cluster with three-dimensional percolation can be clearly seen.

3.3. Connectivity and confinement of water clusters

Using the information obtained from the cluster analysis, quantitative measures of structure in terms of connectivity and confinement of water clusters were further performed. In addition to the percolation information, the connectivity of water clusters was explored by examining the average number of clusters (n_{avg}). Smaller water domain connectivity results in larger n_{avg} values, whereas

1 better connectivity should result in lower n_{avg}. For the normalization of n_{avg}, the connectivity, c_{avg},
2 was defined as

3 $$c_{avg} = \frac{n_{sulfonate} - n_{avg}}{n_{sulfonate} - 1}, \quad (1)$$

4 where $n_{sulfonate}$ is the number of sulfonate groups in the system ($n_{sulfonate}$ = 80 in this work). We
5 assumed that all water clusters were retained by at least one or more sulfonate groups so that the
6 number of water clusters should be always smaller than $n_{sulfonate}$. Therefore, $n_{sulfonate}$ was used as a
7 reference for the possible maximum number of clusters. A poorly connected system, in which
8 water molecules are bound to the independent sulfonate groups to form isolated clusters, results
9 in c = 0, whereas a perfectly connected system, in which all water molecules and sulfonate groups
10 aggregate into a large single cluster, results in c = 1. Figure 6 shows the variations of n_{avg} and c_{avg}
11 as a function of λ. When λ increases, n_{avg} decreases, thus resulting in the increase of c_{avg}. A similar
12 decreasing trend in n_{avg} was observed in the previous study.[44] Specifically, n_{avg} decreases quickly
13 from λ = 3 to λ = 7, which corresponds to the rapid increase of c_{avg} from 40% to 90%,
14 approximately. This suggests the existence of a strong correlation between connectivity and
15 percolation, that is, an increase in the connectivity is significant around and below the percolation
16 threshold (λ < 5.6). At high water contents, a slight decrease in n_{avg} from 2.1 to 1.7, which
17 corresponds to the change in c_{avg} from 97% to 98%, was observed as λ increased from 12 to 20.
18 However, the effect of this change on the proton transport should be negligible because the size
19 of a smaller cluster among two clusters is significantly small by considering the fact that S_{mean}
20 values are 2.7 and 2.0 at λ = 12 and λ = 20, respectively (Figure 3).

21 Although these analyses provide an idea of the connectivity of water domains, they do not directly
22 provide information on the geometry and size of clusters associated with confinement. The

volume and the interfacial surface area of water clusters were calculated to quantify the confinement properties of the water domains. The ratio of the surface area (SA) to water volume (WV) provides a quantitative characteristic of the geometry and size of the water domain. A decrease in the surface-to-volume ratio (SA/WV) indicates that (i) the size of the water domain increases and/or (ii) the shape of the water domain becomes more spherical. The SA/WV ratio can thus be used to compare the morphologies of the water domains in various systems. The surface area of the water domain was calculated using the accessible surface area (ASA) calculation approach based on the Shrake–Rupley algorithm.[49] The accessible surface is created by tracing the center of the spherical probe with a radius of 0.14 nm, which approximates the radius of a water molecule as it rolls along the water domain surface. The water volume was also calculated based on the same assumption that a water molecule has a radius of 0.14 nm and that the water volume can be obtained from the sum of water molecules.

The surface area of the water domains, the water volume, and the SA/WV ratio for various water contents are listed in Table 1. The SA/WV ratio was found to decrease with increasing water content, thus indicating that the water domains (i) have larger sizes and/or (ii) tend to be more spherical. The general trend whereby a decrease in the SA/WV ratio is due to a larger increase in WV rather than due to SA for increasing water contents are comparable with those reported in previous studies.[18, 19] To further clarify the changes in the two characteristics of (i) size and (ii) geometry of the water domain in detail, the SA was evaluated for each cluster size at different water contents. The variations of SA as a function of cluster size for various water contents are shown in Figure 7. For comparison, SA_{sphere}, defined as the surface area of the ideal spherical shape with a given cluster size *S*, is also plotted in Figure 7. For all water contents, SA was found to increase significantly with increasing cluster size, which results in a large difference between SA and SA_{sphere}. At $\lambda = 3$ and $\lambda = 7$ ($S < \sim 600$), a larger increase in SA compared with that seen

above $\lambda = 7$ was observed, suggesting that the growth and aggregation behavior of clusters are different at low- and high-water contents. In Figure 8, we plot the SA_{sphere}-to-SA ratio (SA_{sphere}/SA) as a function of S to characterize the growth behavior of water clusters in different sizes of water domains. A perfect spherical shape of cluster results in $SA_{sphere}/SA = 1$, while SA_{sphere}/SA decreases as the shape of the cluster becomes elongated (less spherical). At $\lambda \leq 7$ ($S < \sim 600$), the SA_{sphere}/SA value decreases rapidly with increasing S, thus indicating that the water domains grow and expand as elongated clusters. This expansion of water domains thus contributes mainly to the increase in the channel length, thereby leading to the connected elongated clusters with a channel-network structure. This is consistent with the percolation behavior at $\lambda = 5.6$, as observed in Section 3.2. At $\lambda > 7$, or above the percolation threshold, the SA_{sphere}/SA elicits a slight increase with increasing S, suggesting that the clusters become somewhat more spherical. However, given that the water domains are percolated and have the channel-network structure in these hydration levels, it seems reasonable to suppose that the channel width of water domains increases, while the elongated structure of clusters is retained. Thus, an increased rate of SA is suppressed compared with that of SA_{sphere}. Therefore, our results suggest that the main contribution of the increase in channel size to the confinement reduction changes with increasing water content from the channel length below the percolation threshold ($\lambda < 5.6$) to the channel width above the percolation threshold ($\lambda > 5.6$). These results are consistent with network morphological models,[50, 51] which consist of a randomly connected network of cylindrical channels or worm-like micelles in polymers, on the basis of various experimental techniques and associated measurements, such as scattering measurements. Our findings of cluster growth behaviors with increasing water contents in terms of connectivity and confinement are consistent with the characterization of three factors of acidity, connectivity, and confinement in the Nafion system using an empirical model[28] based on the effective

medium approximation of percolation theory. Our results provide a more detailed and consistent perspective of cluster characterizations, which support the significance of these three factors.

3.4. Long-time diffusive behaviors of proton and water

To characterize the transport properties of excess protons and water molecules, and to establish their dependence on λ, the self-diffusion coefficients of excess protons and water molecules at different λ values were calculated using their MSDs and Einstein's relation. As it has been discussed previously,[24, 52] diffusion of small molecules (e.g., O_2 and H_2O) in amorphous polymers exhibits subdiffusive or anomalous behavior at the time scale of multiple nanoseconds, which is attributed to the disparity of short-time behavior of small molecules in polymers compared to those in bulk solutions. Therefore, the time scale of tens of nanoseconds is needed, especially at low water concentrations, to determine the long-time diffusivity with statistical certainty.

The MSDs of protons as a function of time are shown in Figure 9 (a). The inset shows the same plots in linear form for $t < 1$ ns for comparison. For an infinite amount of time, the MSD of a diffusing particle scales linearly with time corresponding to long-time diffusion, where the slope of the MSD curve approaches the value of unity in the log–log scale, or the MSD/time curve converges to a constant value. The MSD/time plots of proton and water as a function of time are shown in Figure 9 (b). We found that although the MSDs at high water contents ($\lambda \geq 7$) are linear plots, those at low water contents ($\lambda \leq 5$) do not fully reach the time limit of unity within the timeframe of the 20 ns simulations. Instead, the exponent, $\text{MSD} \propto t^m$, was found to fall in the subdiffusive range of 0.8 to 0.9, which is similar to those observed in the short-time simulations for 1 ns.[24, 28] However, as shown in Figure 9 (b), the MSD/time values decrease

gradually with time and appear to be nearly constant at $t > 5$ ns at low as well as high water contents. This indicates that the changes in the MSD slope become considerably smaller after a 5 ns simulation. Thus, one can reasonably estimate the self-diffusivity using 5 ns of MSD data even though the MSDs are in the nonlinear regime. Similar trends of decreasing MSD slopes with time were reported in a previous study.[24] Therefore, in order to obtain statistically reliable MSDs of 5 ns in duration, a simulation of at least 10 ns is necessary and sufficient to estimate the long-time diffusivity. In addition, an extension of our MSD data for future applicability to a CRW simulation approach,[29] with an additional inclusion of the essential factors in proton transport mechanisms (e.g., a negative correlation between the vehicular and Grotthuss components), would be to predict the long-time diffusivity from the analytical estimation of longer MSDs up to 100 ns. The (subdiffusive) dynamics associated with shorter time scales dominate the motion of the molecules corresponding to free flight within a cluster, which is much faster than the random walk. Thus, the MSD/time values shift upward at the beginning. At lower water contents, since the intrinsic diffusivity (i.e., intracluster diffusivity) becomes relatively large compared to self-diffusivity,[28] the difference between the shorter and longer time scale MSD/time values becomes more significant. One may determine the self-diffusivity from the linear fitting to the MSDs at $t < 1$ ns if the linear forms of MSD plots are used, as shown in the inset of Figure 9 (a). However, this could cause a significant error in the estimation of the diffusion coefficients. This highlights the danger of using the short-time MSD regime ($t < 5$ ns) to determine the long-time diffusion coefficients, particularly at low water contents. For example, if the proton diffusion coefficient is calculated by the linear fitting at $t < 1$ ns (i.e., the linear fitting from 0.5 to 1 ns for example), which is the typical regime for protons used in previous studies of PFSA membrane systems,[20, 22, 23] the diffusion coefficient for $\lambda = 3$ is ~150% larger compared to the long-time counterpart, while that for $\lambda = 20$ it is only ~30%

larger. Consequently, in the present work, the long-time diffusion coefficients of proton and water were calculated from the linear fitting to the MSD curves from 5 to 10 ns. It should be noted, however, that the measurement of the long-time diffusivity associated with the macroscopic degree of multiple cluster network is outside the capability of these simulations. Thus, our results elicited from MD simulations would have to be integrated with a coarse-grained model for further understanding of the relation between the proton transport and the PFSA morphology.

Figure 10 (a) and (b) show the long-time diffusion coefficients of excess protons (D_{H+}) and those of the water molecules (D_{H2O}), respectively. For comparison, the proton diffusion coefficients from experimental measurements,[5] and those obtained with the SCI–MS–EVB model[22] and the classical hydronium ion (nonreactive SPC/Fw H_3O^+) model,[22] are also plotted in Figure 10 (a); the water diffusion coefficients from experimental measurements[5] and those obtained with the classical water (nonreactive SPC/Fw water) model[22] and the analytical model[28] are depicted in Figure 10 (b). As shown in Figure 10 (a), D_{H+} increases with increasing λ values, in which general trends in the experimental data were reproduced by the present model, and a significant improvement in proton diffusion over that seen in the classical hydronium ion model was achieved. When λ is increased from 3 to 7, compared with $\lambda \geq 7$, a larger increase by more than two orders of magnitude is observed, which implies the different behaviors of proton transport below and above the percolation threshold. In this regard, we discussed the direct relationship between proton transport and cluster structure associated with connectivity and confinement in Section 3.4. We also note that in ref 27, the reported diffusion coefficients for the protons in Nafion were too high because the MSD curves were not correctly calculated (and the simulation time was too short for the long-diffusions), although they appeared to be accidentally in good agreement with experimental measurements. It should be

noted that the diffusion coefficients of protons obtained with the SCI–MS–EVB model are calculated by linear fitting at $t < 1$ ns, which may be in the subdiffusive regime and which overestimate the long-time diffusion coefficients, and they are thus used only as a part of the evaluation criteria. In fact, D_{H+} at $\lambda = 5$ obtained with the *a*TS–EVB model appears to be lower than that elicited by the SCI–MS–EVB model. However, if D_{H+} at $\lambda = 5$ is calculated by the linear fitting at $t < 1$ ns with the *a*TS–EVB model, the value of 4.42×10^{-6} cm^2/s can be obtained, which is ~150% larger compared to the long-time diffusion and is comparable with that obtained by the SCI–MS–EVB model. In contrast, D_{H+} values at $\lambda \geq 7$ show better overall agreement with the experiment compared to those for the SCI-MS-EVB model, although the subdiffusive behaviors in the SCI–MS–EVB model may overestimate the D_{H+} values. In addition, as shown in Figure 10 (b), the diffusion coefficients of water molecules were found to be in good agreement quantitatively with the experimental data as well as those obtained using the classical and analytical water models for the studied water contents, there by justifying the validation of the present simulation model. Nevertheless, the values of D_{H+} with the *a*TS–EVB model are still somewhat lower than the values measured experimentally. This is attributed to the essential nature of the lower proton diffusion of the *a*TS–EVB model for which proton diffusion is approximately 40% lower than the experimental value in bulk aqueous water.[31] Moreover, our results do not take into account the large-scale morphological information in membranes that may have an influence on the overall proton transport, which is difficult to be captured in simulations at the atomic level at length-scales spanning tens of nanometers. However, the information obtained from our simulations is still important to understand the proton transport behavior arising from the interplay of proton hopping and vehicular diffusion, which can be bridged into mesoscale simulations[53] to access the scales necessary to investigate the global proton transport.

The influence of water content on proton transport was analyzed further by decomposing the total proton displacement into two different contributions, namely, the vehicular mechanism and the Grotthuss mechanism, using the same approach, as that reported by Peterson and Voth.[21] A sample plot for the total MSD decomposition into the vehicular component and the Grotthuss component at λ = 12 is shown in Figure 11 (a). The smaller total MSD curve compared with the MSDs of either component indicates the anticorrelated nature of the vehicular and Grotthuss motions. In other words, the vehicular and Grotthuss motions tend to move partially in opposite directions, and the cross term thus becomes negative. This anticorrelation behavior agrees with the previous results using the SCI–MS–EVB model,[21] which suggests that the accurate description of the proton transport behavior is achieved using the *a*TS–EVB model.

Figure 11 (b) shows the MSD per one discrete move ($D_{\text{Grotthuss}}$) and continuous move (D_{Vehicle}) in an interval of 1 ps calculated from the linear fitting to the MSDs of each component from 5 to 10 ns. Both $D_{\text{Grotthuss}}$ and D_{Vehicle} increase as λ increases, which indicate that both components contribute to the increase in the total proton diffusion for all water contents. The difference between the total MSD and the sum of the vehicular and Grotthuss components decrease with increasing λ values, thereby indicating that the negative correlation of the two components becomes smaller at higher water contents, which is consistent with the negligible negative correlation in bulk water.[21, 31] To evaluate each component contribution quantitatively, the Grotthuss contribution was calculated as

$$C_{\text{G}} = \frac{D_{\text{Grothuss}}}{D_{\text{Grothuss}} + D_{\text{Vehicle}}}. \quad (2)$$

Figure 11 (c) shows the Grotthuss contribution C_G as a function of λ. The value of C_G increases abruptly from ~50% to ~60% at $\lambda = 7$ but only exhibits a slight increase at higher water contents, thus suggesting that the Grotthuss component becomes more important when crossing the estimated percolation threshold of $\lambda = 5.6$.

3.5. Relationship between proton transport and water cluster structure

To illustrate consistency between the changes in the proton transport and the growth of the cluster network with increasing water content, our findings on percolation, cluster number, surface-to-volume ratio, and proton diffusion coefficient were integrated.

For low water contents, we observe a significant increase by more than almost two orders of magnitude in the proton diffusion and a large increase in the Grotthuss contribution with increasing water contents from $\lambda = 3$ to $\lambda = 7$, as shown Figure 10 (a) and Figure 11 (c). These trends seem to be strongly correlated with a rapid increase in the connectivity c_{avg} from 40% to 90% (Figure 6). In addition, the water domains were found to grow mainly along the channel length as elongated clusters in these water contents, which reduces confinement (Figure 8). Taken together, the expansion of water domains as elongated clusters with increasing water content enhances connectivity and eventually reaches the percolation to form a channel-network structure. Therefore, an increase in connectivity and a decrease in confinement contribute to the enhancement of proton transport, and the percolation threshold can be an important indicator of the transition point associated with cluster growth and the proton transport mechanism.

For high water contents, or above the percolation threshold ($\lambda = 5.6$), we observe smaller increases in the proton diffusion and the Grotthuss contribution compared with those at low water contents. Since the water domains are percolated with a channel-network structure in these hydration levels, connectivity c_{avg} shows little change, whereas confinement is further decreased by the

growth of water domains associated with the channel width. Therefore, an increase in proton diffusivity stems mainly from the decrease in confinement above the percolation threshold.

4. CONCLUSIONS

We have performed a RMD simulation to characterize the relationship between proton transport and water clustering in PEMs. The aims of this study were to: (i) provide an in-depth perspective of distinct cluster growth behaviors below and above the percolation threshold, which influences contributions of connectivity and confinement to proton transport, and (ii) demonstrate applicability of the *a*TS–EVB model to estimate the long-time diffusions, reproduce quantitatively the experimental values of proton/water self-diffusivity, and ascertain the intrinsic nature of proton solvation and transport mechanism observed in the previous RMD simulations.

The proton solvation structure was found to be stabilized in the Eigen-like solvation structure beyond the first solvation shell, while that in the first solvation shell was strongly influenced by the sulfonate groups. Our results, based on the percolation theory, showed that the percolation threshold was λ = 5.6. The connectivity and confinement of water clusters were explored by examining the average number of clusters and the surface-to-volume ratio. The increase in connectivity with increasing water content was found to be significant before the system reached the percolation threshold. The decrease in confinement with increasing water content was identified regardless of water contents. However, the water channels grew and expanded differently below and above the percolation threshold. Our results suggest that below the percolation, the water domains grew along the channel length, which led to the connected, elongated clusters, with a channel-network structure, whereas above the percolation, the channel width of water domains increased while the elongated structure of clusters was retained.

The long-time proton diffusion coefficients were estimated from the MSDs. It was shown that at high water contents, the proton/water long-time diffusivity could be estimated from the linear regime of MSDs obtained based on simulations that spanned at least 10 ns in simulations. Although at low water contents the simulation did not reach the linear regime (i.e., the exponent, MSD $\propto t^m$, fell in a subdiffusive range of 0.8 to 0.9), the slope of the MSD was found to be nearly constant after 5 ns so that one can reasonably estimate the self-diffusivity, which agreed quantitatively with the available experimental data and analytical model. Therefore, a simulation of at least 10 ns is necessary and sufficient to obtain statistically reliable MSDs. In addition, the contributions of the vehicular and Grotthuss mechanisms on the proton transport were analyzed. The results showed that the vehicular and Grotthuss motions elicited anticorrelation behaviors, and the contribution of the Grotthuss mechanism became more important when it crossed the estimated percolation threshold of $\lambda = 5.6$.

The results of the cluster connectivity and confinement and the proton transport were integrated to illustrate the consistent outlook of the relationship between the water cluster structure and proton transport. Considered collectively, the results suggest that an increase in connectivity and a decrease in confinement contribute to the enhancement of proton transport below the percolation threshold, while a decrease in confinement is predominant for an increase in proton diffusion above the percolation threshold. The percolation threshold can thus be an important indicator of the transition point associated with cluster growth and the proton transport mechanism.

The present study provides direct, quantitative evidence of the influence of water cluster structures on proton transport properties and demonstrates the suitability of the *a*TS–EVB model to provide accurate descriptions of long-time proton transport properties within the simplicity of the theoretical framework. By taking advantage of the present approach, future

research will focus on further understandings and characterizations of proton transport properties in PEMs using different types of materials as well as PFSA membranes.

ACKNOWLEDGMENT

This work was supported by the New Energy and Industrial Technology Development Organization (NEDO) of Japan and the Japan Society for the Promotion of Science (JSPS) KAKENHI Grant Number JP17K14600. It was performed, in part, using the supercomputer of the Institute of Fluid Science (IFS) of Tohoku University.

REFERENCES

(1) Wang, Y.; Chen, K. S.; Mishler, J.; Cho, S. C.; Adroher, X. C., A Review of Polymer Electrolyte Membrane Fuel Cells: Technology, Applications, and Needs on Fundamental Research. *Appl. Energy* **2011**, *88*, 981-1007.

(2) Kusoglu, A.; Weber, A. Z., New Insights into Perfluorinated Sulfonic-Acid Ionomers. *Chem. Rev.* **2017**, *117*, 987-1104.

(3) D'Epifanio, A.; Navarra, M. A.; Weise, F. C.; Mecheri, B.; Farrington, J.; Licoccia, S.; Greenbaum, S., Composite Nafion/Sulfated Zirconia Membranes: Effect of the Filler Surface Properties on Proton Transport Characteristics. *Chem. Mater.* **2010**, *22*, 813-821.

(4) Zawodzinski, T. A.; Neeman, M.; Sillerud, L. O.; Gottesfeld, S., Determination of Water Diffusion Coefficients in Perfluorosulfonate Ionomeric Membranes. *J. Phys. Chem.* **1991**, *95*, 6040-6044.

(5) Ochi, S.; Kamishima, O.; Mizusaki, J.; Kawamura, J., Investigation of Proton Diffusion in Nafion (R) 117 Membrane by Electrical Conductivity and NMR. *Solid State Ionics* **2009**, *180*, 580-584.

(6) Kidena, K.; Ohkubo, T.; Takimoto, N.; Ohira, A., Pfg-Nmr Approach to Determining the Water Transport Mechanism in Polymer Electrolyte Membranes Conditioned at Different Temperatures. *Eur. Polym. J.* **2010**, *46*, 450-455.

(7) Agmon, N., The Grotthuss Mechanism. *Chem. Phys. Lett.* **1995**, *244*, 456-462.

(8) Devanathan, R.; Venkatnathan, A.; Dupuis, M., Atomistic Simulation of Nafion Membrane: I. Effect of Hydration on Membrane Nanostructure. *J. Phys. Chem. B* **2007**, *111*, 8069-8079.

(9) Cui, S. T.; Liu, J. W.; Selvan, M. E.; Keffer, D. J.; Edwards, B. J.; Steele, W. V., A Molecular Dynamics Study of a Nafion Polyelectrolyte Membrane and the Aqueous Phase Structure for Proton Transport. *J. Phys. Chem. B* **2007**, *111*, 2208-2218.

(10) Jang, S. S.; Molinero, V.; Cagin, T.; Goddard, W. A., Nanophase-Segregation and Transport in Nafion 117 from Molecular Dynamics Simulations: Effect of Monomeric Sequence. *J. Phys. Chem. B* **2004**, *108*, 3149-3157.

(11) Karo, J.; Aabloo, A.; Thomas, J. O.; Brandell, D., Molecular Dynamics Modeling of Proton Transport in Nafion and Hylton Nanostructures. *J. Phys. Chem. B* **2010**, *114*, 6056-6064.

(12) Knox, C. K.; Voth, G. A., Probing Selected Morphological Models of Hydrated Nafion Using Large-Scale Molecular Dynamics Simulations. *J. Phys. Chem. B* **2010**, *114*, 3205-3218.

(13) Komarov, P. V.; Khalatur, P. G.; Khokhlov, A. R., Large-Scale Atomistic and Quantum-Mechanical Simulations of a Nafion Membrane: Morphology, Proton Solvation and Charge Transport. *Beilstein J Nanotech* **2013**, *4*, 567-587.

(14) Spohr, E., Monte Carlo Simulations of a Simple Lattice Model of Polymer Electrolyte Membranes. *J. Mol. Liq.* **2007**, *136*, 288-293.

(15) Mabuchi, T.; Tokumasu, T., Effect of Bound State of Water on Hydronium Ion Mobility in Hydrated Nafion Using Molecular Dynamics Simulations. *J. Chem. Phys.* **2014**, *141*, 104904.

(16) Kornyshev, A. A.; Spohr, E., Proton Transport in Polymer Electrolyte Membranes Using Theory and Classical Molecular Dynamics. In *Device and Materials Modeling in Pem Fuel Cells*, Paddison, S.; Promislow, K., Eds. Springer Berlin Heidelberg: 2009; Vol. 113, pp 349-363.

(17) Devanathan, R.; Dupuis, M., Insight from Molecular Modelling: Does the Polymer Side Chain Length Matter for Transport Properties of Perfluorosulfonic Acid Membranes? *Phys. Chem. Chem. Phys.* **2012**, *14*, 11281-11295.

(18) Kuo, A.-T.; Shinoda, W.; Okazaki, S., Molecular Dynamics Study of the Morphology of Hydrated Perfluorosulfonic Acid Polymer Membranes. *J. Phys. Chem. C* **2016**, *120*, 25832-25842.

(19) Liu, J.; Suraweera, N.; Keffer, D. J.; Cui, S.; Paddison, S. J., On the Relationship between Polymer Electrolyte Structure and Hydrated Morphology of Perfluorosulfonic Acid Membranes. *J. Phys. Chem. C* **2010**, *114*, 11279-11292.

(20) Feng, S.; Voth, G. A., Proton Solvation and Transport in Hydrated Nafion. *J. Phys. Chem. B* **2011**, *115*, 5903-5912.

(21) Petersen, M. K.; Voth, G. A., Characterization of the Solvation and Transport of the Hydrated Proton in the Perfluorosulfonic Acid Membrane Nafion. *J. Phys. Chem. B* **2006**, *110*, 18594-18600.

(22) Tse, Y.-L. S.; Herring, A. M.; Kim, K.; Voth, G. A., Molecular Dynamics Simulations of Proton Transport in 3m and Nafion Perfluorosulfonic Acid Membranes. *J. Phys. Chem. C* **2013**, *117*, 8079-8091.

(23) Savage, J.; Tse, Y.-L. S.; Voth, G. A., Proton Transport Mechanism of Perfluorosulfonic Acid Membranes. *J. Phys. Chem. C* **2014**, *118*, 17436-17445.

(24) Savage, J.; Voth, G. A., Persistent Subdiffusive Proton Transport in Perfluorosulfonic Acid Membranes. *J. Phys. Chem. Lett.* **2014**, *5*, 3037-3042.

(25) Seeliger, D.; Hartnig, C.; Spohr, E., Aqueous Pore Structure and Proton Dynamics in Solvated Nafion Membranes. *Electrochim. Acta* **2005**, *50*, 4234-4240.

(26) Spohr, E.; Commer, P.; Kornyshev, A. A., Enhancing Proton Mobility in Polymer Electrolyte Membranes: Lessons from Molecular Dynamics Simulations. *J. Phys. Chem. B* **2002**, *106*, 10560-10569.

(27) Mabuchi, T.; Tokumasu, T., Molecular Dynamics Simulation of Proton Transport in Polymer Electrolyte Membrane. *J. Nanosci. Nanotechnol.* **2015**, *15*, 2958-2963.

(28) Esai Selvan, M.; Calvo-Muñoz, E.; Keffer, D. J., Toward a Predictive Understanding of Water and Charge Transport in Proton Exchange Membranes. *J. Phys. Chem. B* **2011**, *115*, 3052-3061.

(29) Calvo-Muñoz, E. M.; Selvan, M. E.; Xiong, R.; Ojha, M.; Keffer, D. J.; Nicholson, D. M.; Egami, T., Applications of a General Random-Walk Theory for Confined Diffusion. *Phys. Rev. E* **2011**, *83*, 011120.

(30) Walbran, S.; Kornyshev, A. A., Proton Transport in Polarizable Water. *J. Chem. Phys.* **2001**, *114*, 10039-10048.

(31) Mabuchi, T.; Fukushima, A.; Tokumasu, T., A Modified Two-State Empirical Valence Bond Model for Proton Transport in Aqueous Solutions. *J. Chem. Phys.* **2015**, *143*, 014501.

(32) Schmitt, U. W.; Voth, G. A., The Computer Simulation of Proton Transport in Water. *J. Chem. Phys.* **1999**, *111*, 9361-9381.

(33) Wang, C.; Clark, J. K.; Kumar, M.; Paddison, S. J., An Ab Initio Study of the Primary Hydration and Proton Transfer of Cf_3so_3h and $Cf_3o(Cf_2)_2so_3h$: Effects of the Hybrid Functional and Inclusion of Diffuse Functions. *Solid State Ionics* **2011**, *199*, 6-13.

(34) Li, T.; Wlaschin, A.; Balbuena, P. B., Theoretical Studies of Proton Transfer in Water and Model Polymer Electrolyte Systems. *Ind. Eng. Chem. Res.* **2001**, *40*, 4789-4800.

(35) Jang, S. S.; Blanco, M.; Goddard, W. A.; Caldwell, G.; Ross, R. B., The Source of Helicity in Perfluorinated N-Alkanes. *Macromolecules* **2003**, *36*, 5331-5341.

(36) Hofmann, D. W. M.; Kuleshova, L.; D'Aguanno, B.; Di Noto, V.; Negro, E.; Conti, F.; Vittadello, M., Investigation of Water Structure in Nafion Membranes by Infrared Spectroscopy and Molecular Dynamics Simulation. *J. Phys. Chem. B* **2009**, *113*, 632-639.

(37) Yan, L.; Balbuena, P. B.; Seminario, J. M., Perfluorobutane Sulfonic Acid Hydration and Interactions with O2 Adsorbed on Pt3. *J. Phys. Chem. A* **2006**, *110*, 4574-4581.

(38) Essmann, U.; Perera, L.; Berkowitz, M. L.; Darden, T.; Lee, H.; Pedersen, L. G., A Smooth Particle Mesh Ewald Method. *J. Chem. Phys.* **1995**, *103*, 8577-8593.

(39) Tuckerman, M.; Berne, B. J.; Martyna, G. J., Reversible Multiple Time Scale Molecular-Dynamics. *J. Chem. Phys.* **1992**, *97*, 1990-2001.

(40) Hoover, W. G., Canonical Dynamics: Equilibrium Phase-Space Distributions. *Phys. Rev. A* **1985**, *31*, 1695-1697.

(41) Nosé, S., Constant Temperature Molecular Dynamics Methods. *Prog. Theor. Phys. Supp.* **1991**, *103*, 1-46.

(42) Andersen, H. C., Molecular Dynamics Simulations at Constant Pressure and/or Temperature. *J. Chem. Phys.* **1980**, *72*, 2384-2393.

(43) Stauffer, D.; Aharony, A., *Introduction to Percolation Theory*. Taylor & Francis: 1994.

(44) Devanathan, R.; Venkatnathan, A.; Rousseau, R.; Dupuis, M.; Frigato, T.; Gu, W.; Helms, V., Atomistic Simulation of Water Percolation and Proton Hopping in Nafion Fuel Cell Membrane. *J. Phys. Chem. B* **2010**, *114*, 13681-13690.

(45) Brovchenko, I.; Krukau, A.; Oleinikova, A.; Mazur, A. K., Ion Dynamics and Water Percolation Effects in DNA Polymorphism. *J. Am. Chem. Soc.* **2008**, *130*, 121-131.

(46) Oleinikova, A.; Brovchenko, I.; Geiger, A.; Guillot, B., Percolation of Water in Aqueous Solution and Liquid–Liquid Immiscibility. *J. Chem. Phys.* **2002**, *117*, 3296-3304.

(47) Partay, L. B.; Jedlovszky, P.; Brovchenko, I.; Oleinikova, A., Formation of Mesoscopic Water Networks in Aqueous Systems. *Phys. Chem. Chem. Phys.* **2007**, *9*, 1341-1346.

(48) Lu, Z. J.; Polizos, G.; Macdonald, D. D.; Manias, E., State of Water in Perfluorosulfonic Ionomer (Nafion 117) Proton Exchange Membranes. *J. Electrochem. Soc.* **2008**, *155*, B163-B171.

(49) Shrake, A.; Rupley, J. A., Environment and Exposure to Solvent of Protein Atoms. Lysozyme and Insulin. *J. Mol. Biol.* **1973**, *79*, 351-371.

(50) Kim, M. H.; Glinka, C. J.; Grot, S. A.; Grot, W. G., Sans Study of the Effects of Water Vapor Sorption on the Nanoscale Structure of Perfluorinated Sulfonic Acid (Nafion) Membranes. *Macromolecules* **2006**, *39*, 4775-4787.

(51) Kreuer, K. D., On the Development of Proton Conducting Polymer Membranes for Hydrogen and Methanol Fuel Cells. *J. Membr. Sci.* **2001**, *185*, 29-39.

(52) Mullerplathe, F.; Rogers, S. C.; Vangunsteren, W. F., Computational Evidence for Anomalous Diffusion of Small Molecules in Amorphous Polymers. *Chem. Phys. Lett.* **1992**, *199*, 237-243.

(53) Jorn, R.; Voth, G. A., Mesoscale Simulation of Proton Transport in Proton Exchange Membranes. *J. Phys. Chem. C* **2012**, *116*, 10476-10489.

FIGURE AND TABLE CAPTIONS

Figure 1. (a) RDFs between a sulfur atom and a hydronium oxygen atom ($g_{S–Oh}$) at various water contents. (b) RDF and coordination number (solid and dashed lines) for water oxygen atoms around the hydronium oxygen atom ($g_{Oh–Ow}$) at $\lambda = 7$. The black and red lines denote the hydronium ions within and outside the first solvation shell, respectively.

Figure 2. Cluster size distribution, n_s, defined as the probability of finding a cluster size of S (the number of hydronium ions and water molecules in a cluster) at various values of λ. The solid line represents the universal power law slope of $\tau = 2.19$ at the three-dimensional percolation threshold.

Figure 3. Mean size of clusters, S_{mean} (with the largest cluster excluded), as a function of λ.

Figure 4. Probability R of finding an infinite cluster as a function of λ. The solid line represents the fit to Boltzmann's sigmoidal function.

Figure 5. Snapshots of the water clusters at (a) $\lambda = 5$, (b) $\lambda = 7$, and (c) $\lambda = 12$. For clarity, each cluster is shown in a different color (the largest cluster is shown in white), while the Nafion chains are not shown.

Figure 6. Average number of clusters, n_{avg} and average connectivity, c_{avg}, defined by Eq. (1) as a function of λ.

Figure 7. Surface area (SA) of water domains as a function of cluster size *S* at various water contents. For comparison, SA_{sphere} is also plotted, defined as the surface area of the ideal spherical shape with a given cluster size *S*, is also plotted.

Figure 8. Plot of the SA_{sphere}-to-SA ratio (SA_{sphere}/SA) as a function of *S*.

Figure 9. (a) MSDs of protons as a function of time plotted at various λ values on a log–log scale. The inset shows the same plots in linear form for $t < 1$ ns. Dashed lines denote $\text{MSD} \propto t^m$ of $m = 1.0$ (black line) and 0.8 (red line). (b) MSD/time of protons as a function of time at various λ values on a log–log scale. Dashed lines show the diffusion coefficients calculated from the linear fitting to the MSD curves from 5 ns to 10 ns.

Figure 10. (a) Long-time diffusion coefficients of protons as a function of λ. (b) Long-time diffusion coefficients of water molecules as a function of λ. The experimental data were obtained from Ochi et al.[5] Simulated results relevant to the SCI–MS–EVB model and the classical models were obtained from Tse et al.[22] The analytical model of water was obtained from Selvan et al.[28] The diffusion coefficients of protons obtained using the SCI–MS–EVB model are calculated in the subdiffusive regime (the linear fitting at $t < 1$ ns).

Figure 11. (a) A sample plot for the total proton MSD decomposed into the vehicular component and Grotthuss component at $\lambda = 12$ as a function of time. (b) MSD for discrete move ($D_{\text{Grotthuss}}$) and continuous move (D_{Vehicle}) in 1 ps

interval as a function of λ. (c) Grotthuss contribution, C_G, defined by Eq. (2) as a function of λ.

Table 1. Surface area (SA) and volume (WV) of water domains, and surface-to-volume ratio (SA/WV) at different water contents.

TABLES

Table 1

Water content λ	Surface area [nm^2]	Volume [nm^3]	SA/WV [nm^{-1}]
3	120.90	2.76	43.83
5	136.96	4.60	29.79
7	145.50	6.44	22.60
12	158.83	11.03	14.39
20	179.80	18.39	9.78

FIGURES

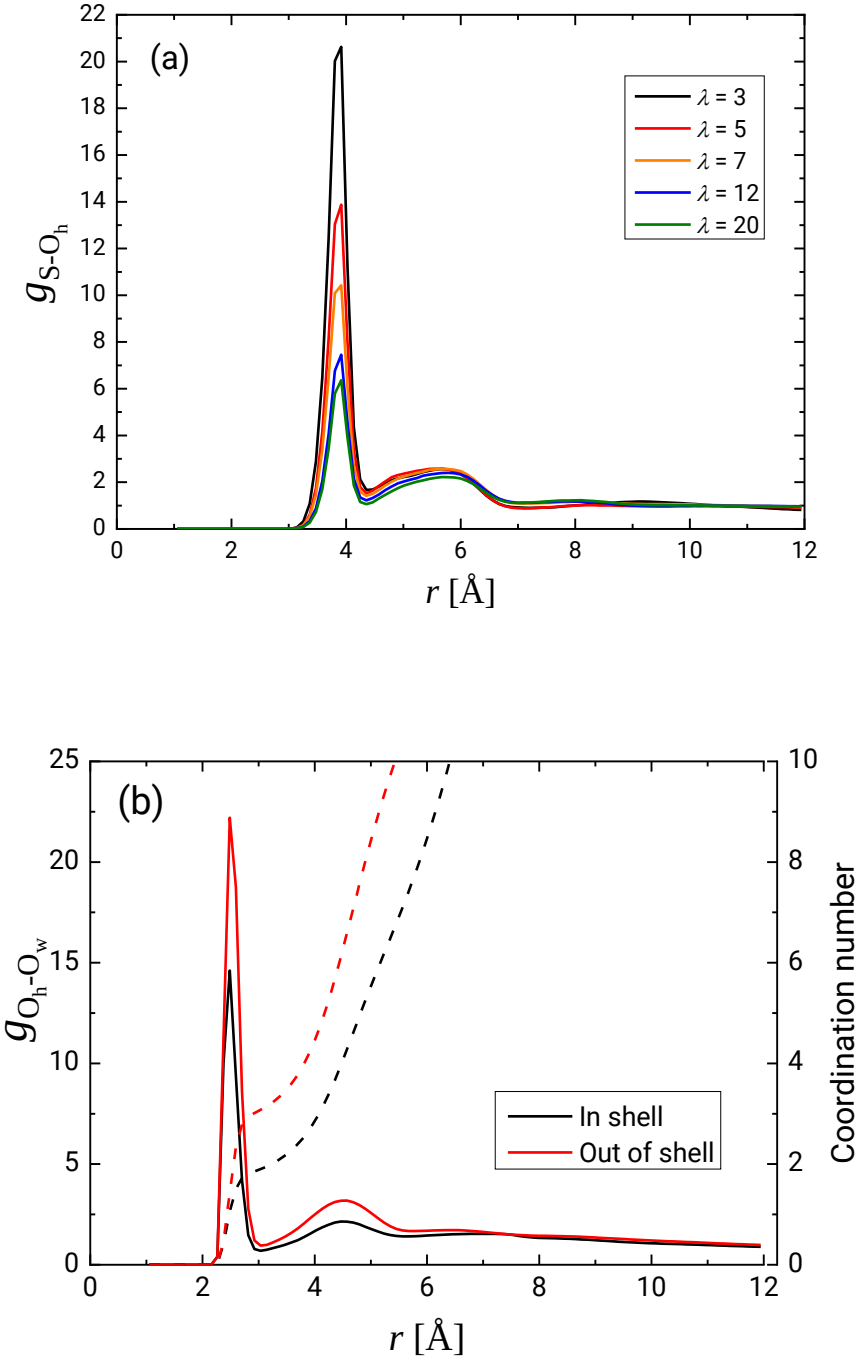

Figure 1

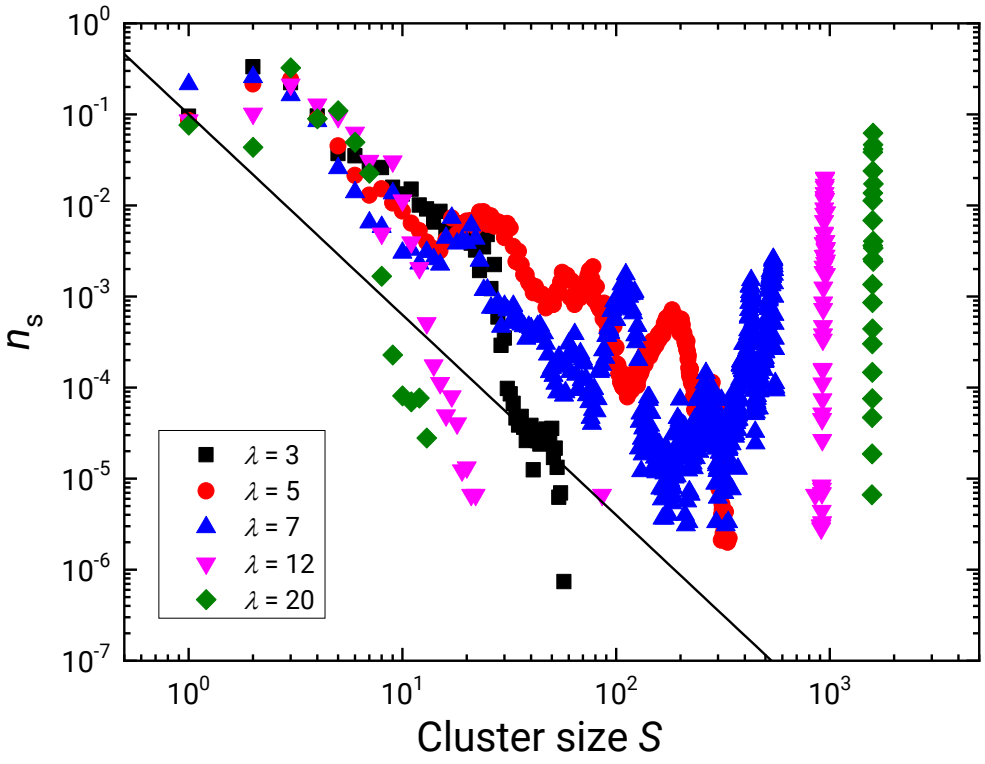
10^0
10^{-1}
10^{-2}
10^{-3}
10^{-4}
10^{-5}
10^{-6}
10^{-7}
n_s
10^0
10^1
10^2
10^3
Cluster size S
$\lambda = 3$
$\lambda = 5$
$\lambda = 7$
$\lambda = 12$
$\lambda = 20$

Figure 2

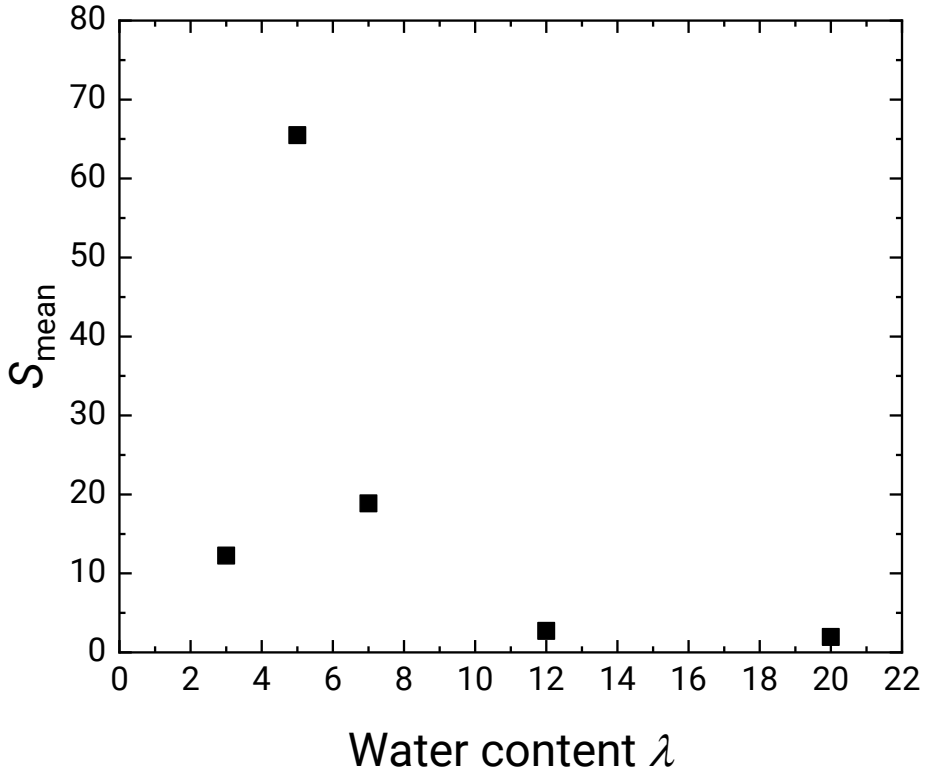
80
70
60
50
40
30
20
10
0
S_{mean}
0
2
4
6
8
10
12
14
16
18
20
22
Water content λ

Figure 3

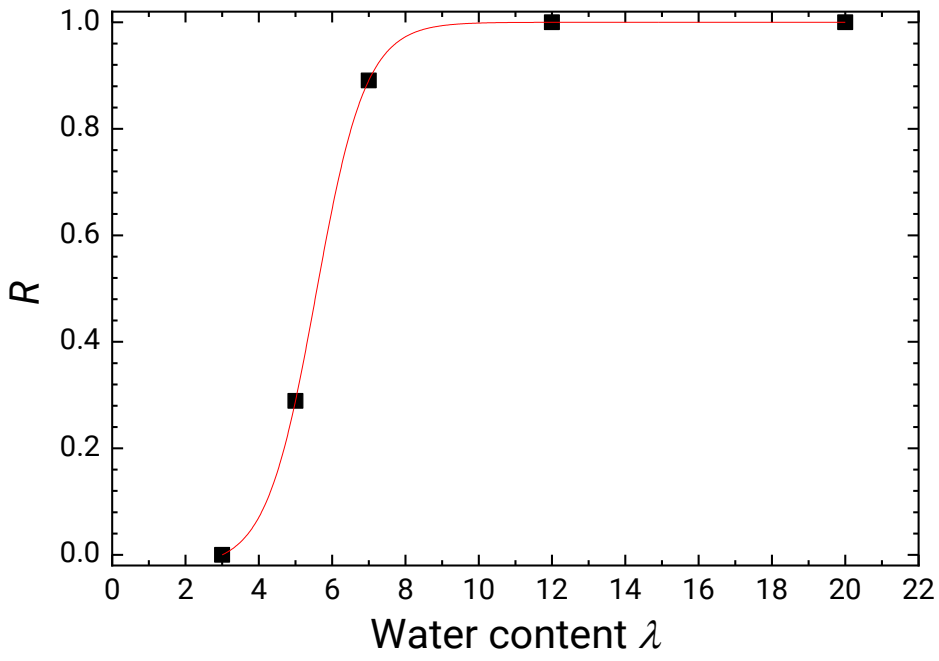

Figure 4

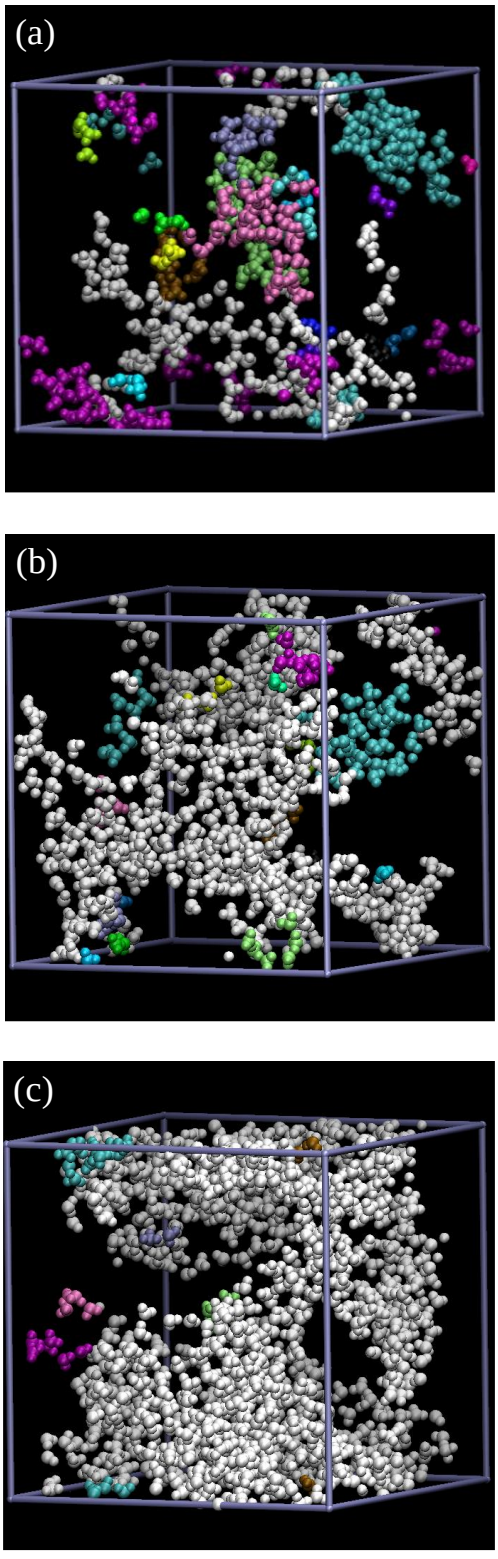

Figure 5

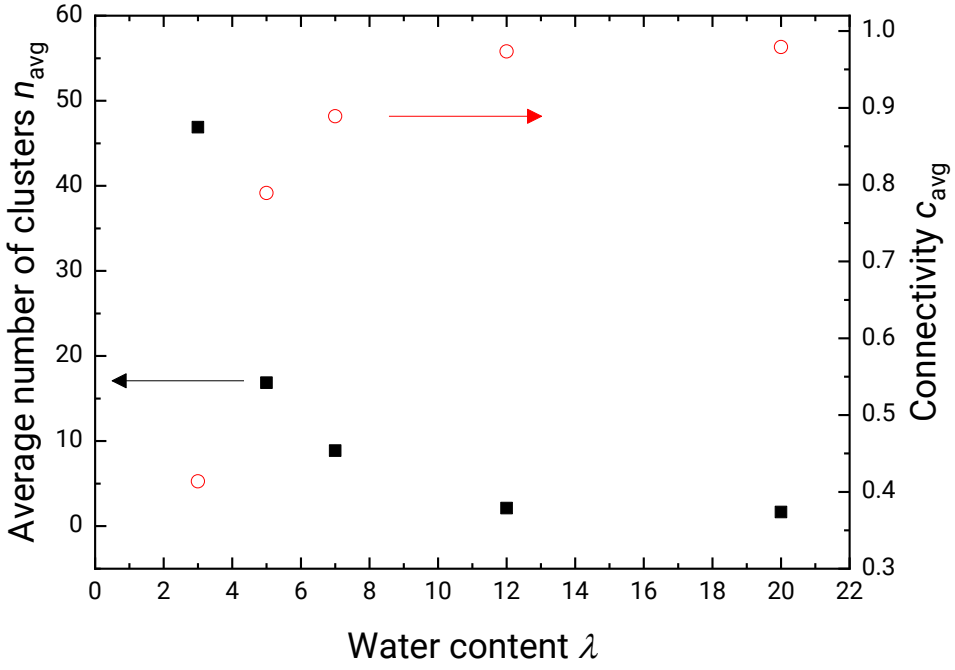
Average number of clusters n_{avg}
Connectivity c_{avg}
Water content λ
0
10
20
30
40
50
60
0.3
0.4
0.5
0.6
0.7
0.8
0.9
1.0
0
2
4
6
8
10
12
14
16
18
20
22

Figure 6

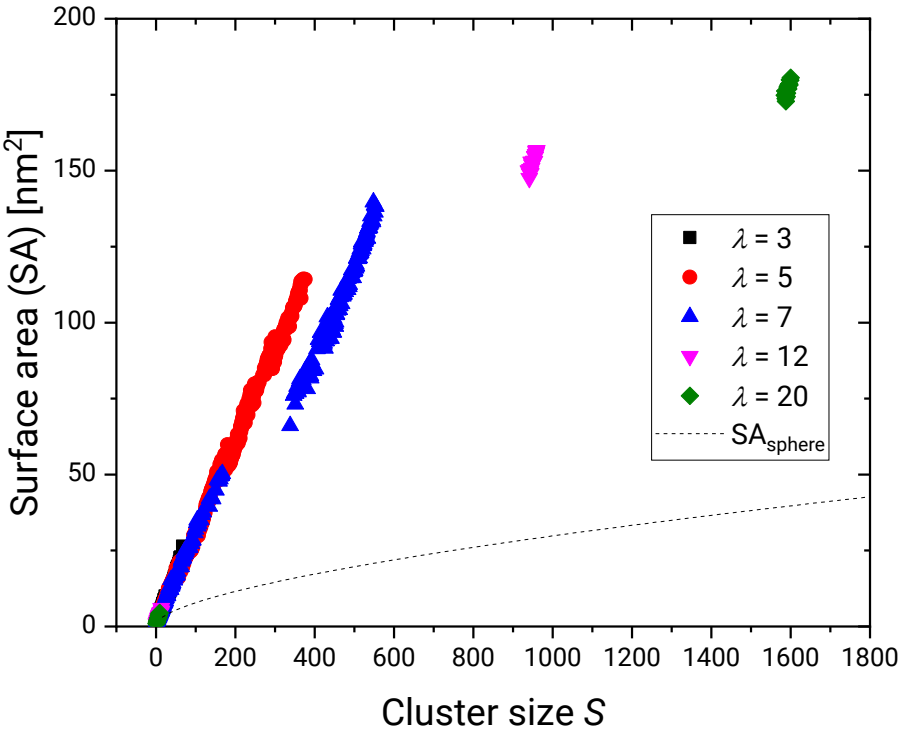
Surface area (SA) [nm^2]
Cluster size S
0
50
100
150
200
0
200
400
600
800
1000
1200
1400
1600
1800
λ = 3
λ = 5
λ = 7
λ = 12
λ = 20
SA$_{sphere}$

Figure 7

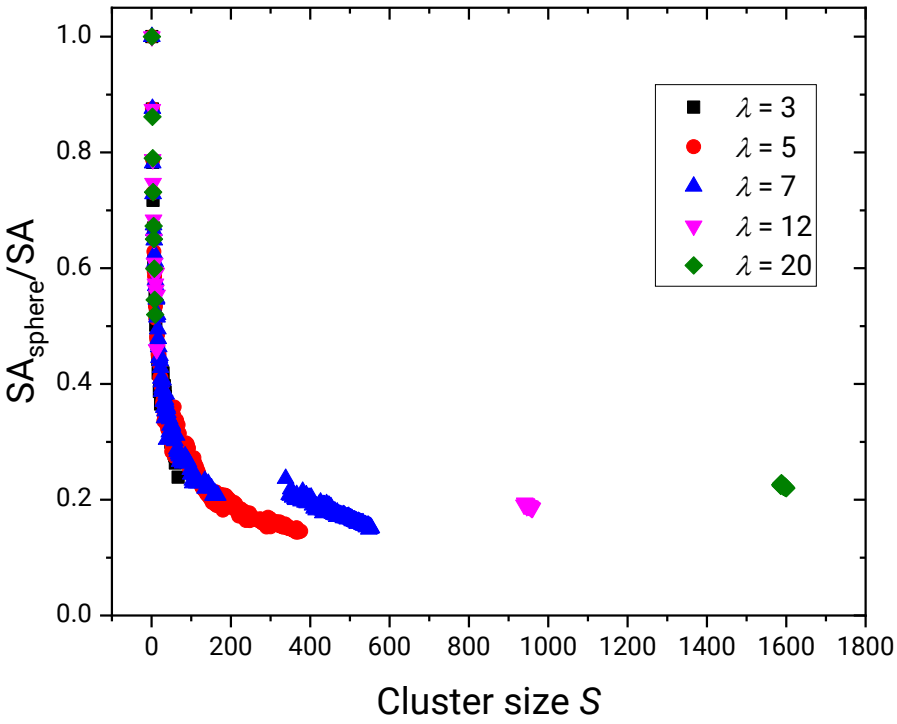
1.0
0.8
0.6
0.4
0.2
0.0
SA$_{sphere}$/SA
0
200
400
600
800
1000
1200
1400
1600
1800
Cluster size S
λ = 3
λ = 5
λ = 7
λ = 12
λ = 20

Figure 8

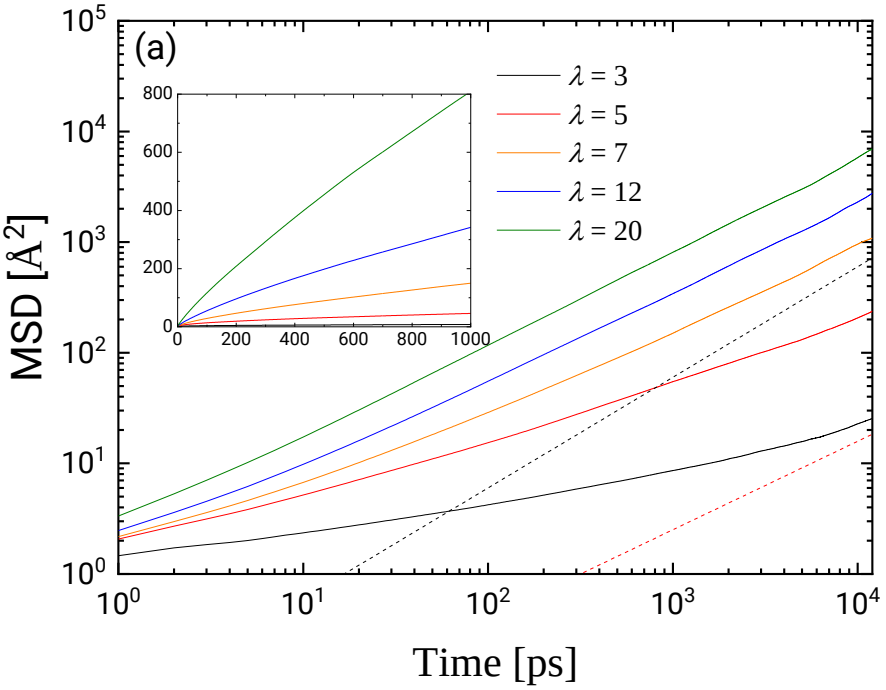
(a)
MSD [Å^2]
Time [ps]
λ = 3
λ = 5
λ = 7
λ = 12
λ = 20

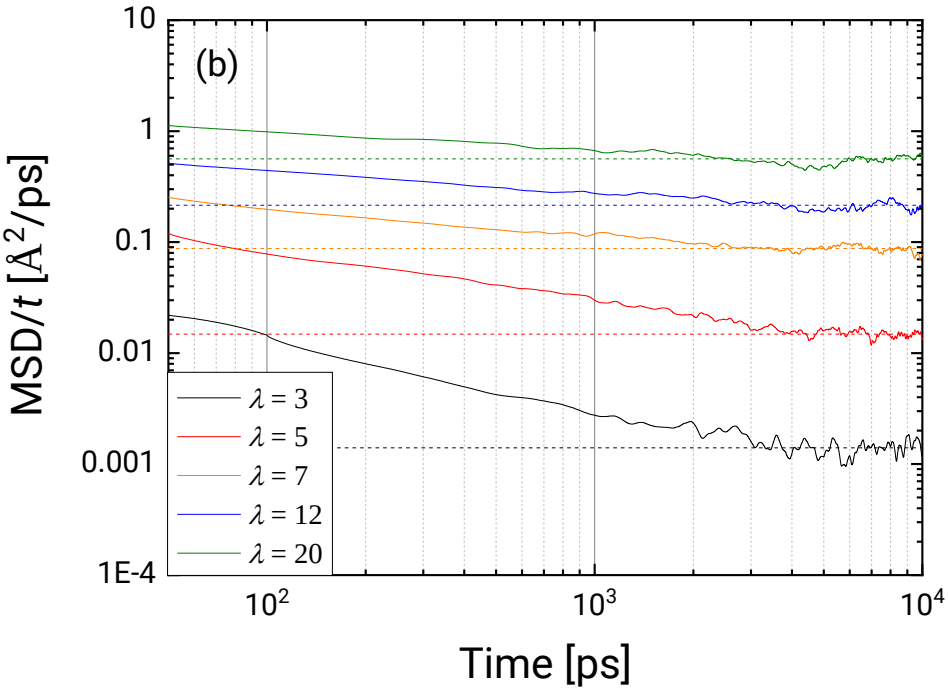
(b)
MSD/t [Å^2/ps]
Time [ps]
λ = 3
λ = 5
λ = 7
λ = 12
λ = 20

Figure 9

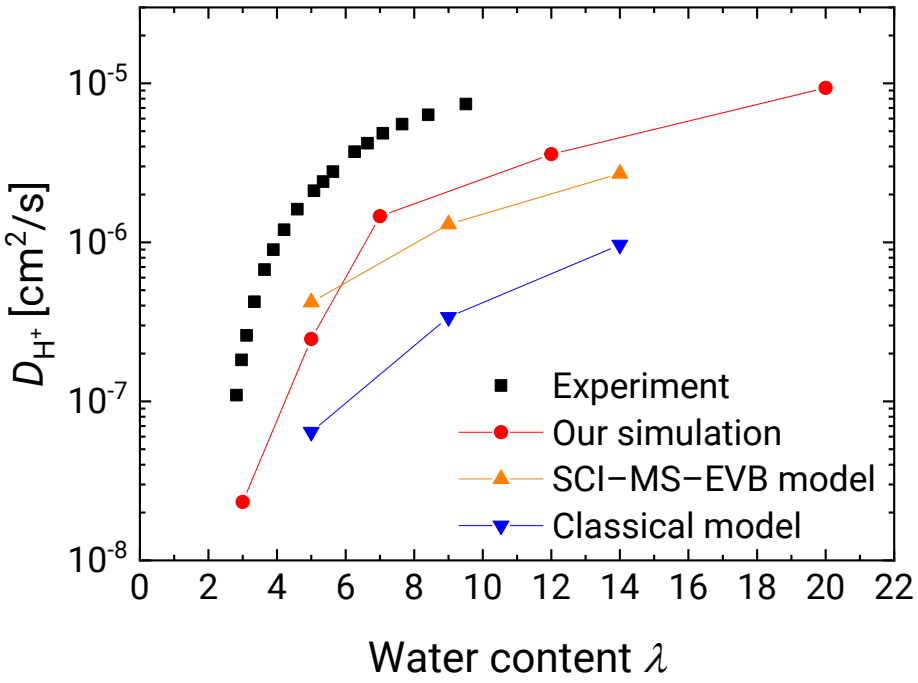
D_{H^+} [cm^2/s]
10^{-5}
10^{-6}
10^{-7}
10^{-8}
0 2 4 6 8 10 12 14 16 18 20 22
Water content λ
Experiment
Our simulation
SCI–MS–EVB model
Classical model

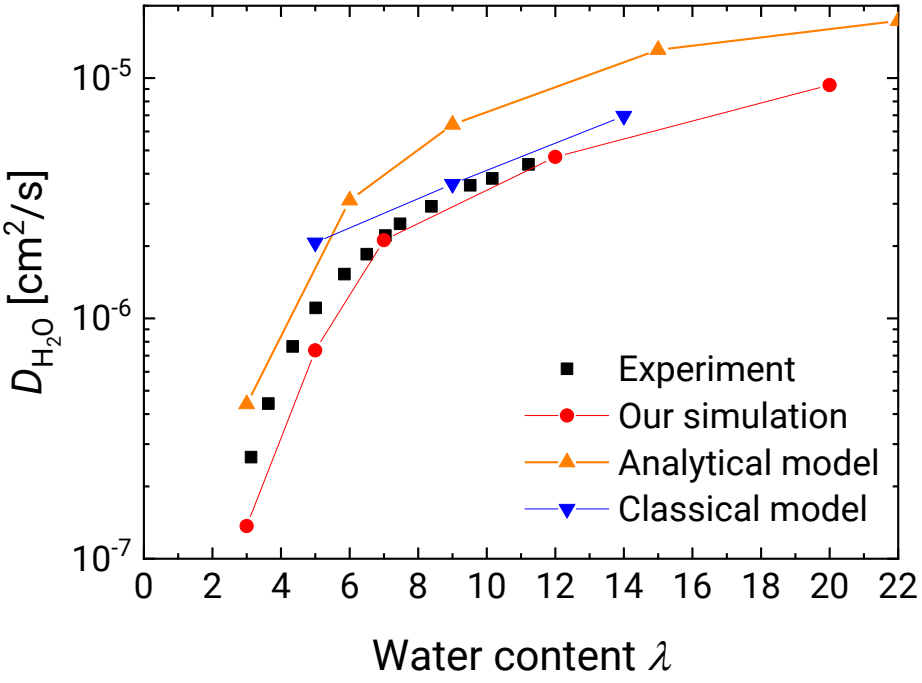
D_{H_2O} [cm^2/s]
10^{-5}
10^{-6}
10^{-7}
0 2 4 6 8 10 12 14 16 18 20 22
Water content λ
Experiment
Our simulation
Analytical model
Classical model

Figure 10

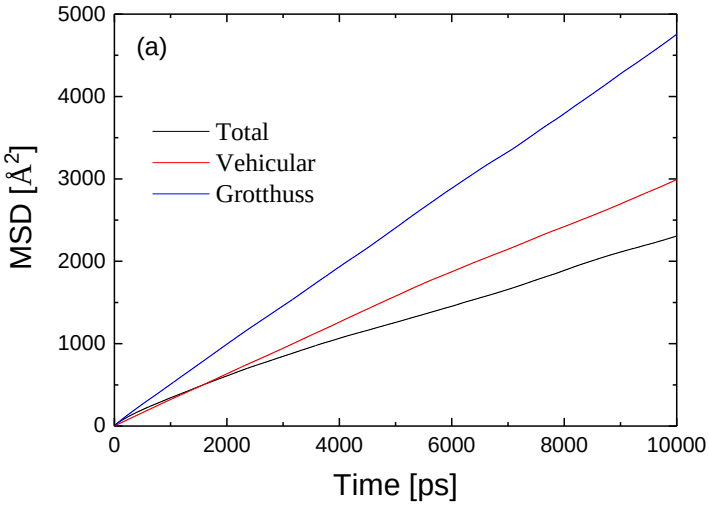
(a)
Total
Vehicular
Grotthuss
MSD [Å^2]
Time [ps]
0
1000
2000
3000
4000
5000
0
2000
4000
6000
8000
10000

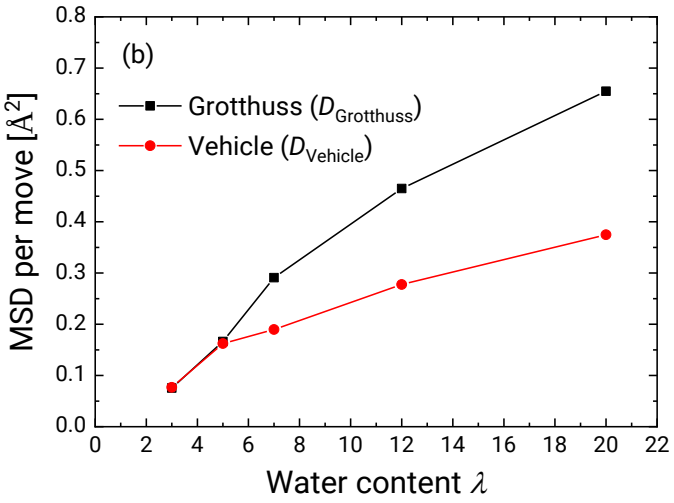
(b)
Grotthuss ($D_{Grotthuss}$)
Vehicle ($D_{Vehicle}$)
MSD per move [Å^2]
Water content λ
0.0
0.1
0.2
0.3
0.4
0.5
0.6
0.7
0.8
0
2
4
6
8
10
12
14
16
18
20
22

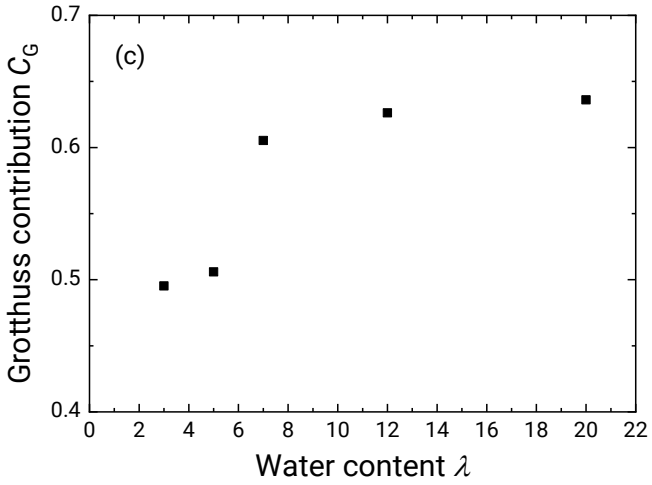
(c)
Grotthuss contribution C_G
Water content λ
0.4
0.5
0.6
0.7
0
2
4
6
8
10
12
14
16
18
20
22

Figure 11

TOC Graphic